August 2020

Exploiting the Nonlinear Stiffness of Origami Folding to Enhance Robotic Jumping Performance

Samuel Reese Allison
Clemson University, allisonr1214@gmail.com

EXPLOITING THE NONLINEAR STIFFNESS OF ORIGAMI FOLDING TO ENHANCE ROBOTIC JUMPING PERFORMANCE

A Thesis
Presented to
the Graduate School of
Clemson University

In Partial Fulfillment
of the Requirements for the Degree
Master of Science
Mechanical Engineering

by
Samuel Reese Allison
August 2020

Accepted by:
Dr. Suyi Li, Committee Chair
Dr. Phanindra Tallapragada
Dr. Georges Fadel

Abstract

This research investigates the effects of using origami folding techniques to develop a nonlinear jumping mechanism with optimized dynamic performance. A previous theoretical investigation has shown the benefits of using a nonlinear spring element compared to a linear spring for improving the dynamic performance of a jumper. This study sets out to experimentally verify the effectiveness of utilizing nonlinear stiffness to achieve optimized jumping performance. The Tachi-Miura Polyhedron (TMP) origami structure is used as the nonlinear energy-storage element connecting two end-point masses. The TMP bellow exhibits a "strain-softening" nonlinear force-displacement behavior resulting in an increased energy storage compared to a linear spring. The geometric parameters of the structure are optimized to improve air-time and maximum jumping height. An additional TMP structure was designed to exhibit a close-to-linear force-displacement response to serve as the representative linear spring element. A critical challenge in this study is to minimize the hysteresis and energy loss of TMP during its compression stage before jumping. To this end, plastically annealed lamina emergent origami (PALEO) concept is used to modify the creases of the structure in order to reduce hysteresis during the compression cycle. PALEO works by increasing the folding limit before plastic deformation occurs, thus improving the energy retention of the structure. Steel shim stock are secured to the facets of the TMP structure to serve as end-point masses, and the air-time and jumping height of both structures are measured and compared. The nonlinear TMP structure achieves roughly 9% improvement in air-time and a 12% improvement in jumping height when compared to the linear TMP structure. These results validate the theoretical benefits of utilizing nonlinear spring elements in jumping mechanisms and can lead to improved performance in dynamic systems which rely on springs as a method of energy storage and can lead to emergence of a new generation of more efficient jumping mechanisms with optimized performance in the future.

Acknowledgments

Table of Contents

List of Tables

List of Figures

Chapter 1

Introduction

The advent of robotics technology has allowed for exponential growth in terms of applications in a multitude of industries. Robots have been critical to the development of large-scale manufacturing [1], as well as the energy, food, and agriculture industries [2–5], education [6, 7], and medical care [8, 9]. Additionally, the ability to send robots into hazardous environments in place of humans has seen tremendous use in military applications [10, 11] and search and rescue operations [12, 13]. Robots sent into the field often encounter difficult terrain, such as volcano exploration or coal extraction, opening opportunities for research into various modes of locomotion to navigate unpredictable landscapes [14]. Ground-contact-based locomotion can be separated into five main categories of movement: wheeled robots, tracked robots, snake robots, legged robots, and wheel-legged robots [14]. While each category has distinct advantages in certain applications, legged robots are of particular interest in rough terrain due to their ability to gain discrete footholds on a variety of surfaces and can traverse steep inclines [14–16].

The drawback of working with legged robots arises in the complexity of the control schemes, especially when working with multi-leg mechanisms requiring coordination between the limbs [17]. Therefore, a large number of researchers have been focusing on single-legged jumping systems in an effort to simplify the control strategies [16, 18–20]. The energy storage mechanism used in a jumping robot is of particular interest due to the direct correlation between the amount of energy stored in the mechanism and the jumping performance of the robot [19, 21]. To this end, researchers have investigated various methods for storing and releasing energy in a jumping robot. In addition to the traditional spring devices [22–24], studies have been conducted on the efficacy of pneumatic devices

[25] as well as custom elastic elements in which unique mechanisms act as nonlinear energy storage devices to generate desirable nonlinear jumping dynamics [26, 27].

Various aspects of nonlinear jumping mechanisms have been studied for their potential benefits to the overall jumping performance of a single-legged jumper. Yamada *et. al.* exploited the snap-through buckling effect of a closed elastica to store greater amounts of energy, leading to increased height and distance achieved by their robot [27, 28]. Fiorini *et. al.* were able to design a jumping mechanism with a nonlinear force response curve through the use of a 6-bar linkage coupled with gears at the joints [29]. Additionally, Sadeghi *et. al.* showed that through the use of "strain-softening" techniques, a jumping mechanism composed of a generic nonlinear elastic element can increase the initial stored energy and consequently create higher jumps in terms of center of gravity and ground clearance with a negligible penalty to efficiency [21]. The results from [21] are based on non-dimensional numerical and analytical results, indicating that different types of nonlinear jumping mechanisms can be used to improve dynamic performance. The objective of this study is to determine to what extent origami can be used as the nonlinear elastic element in a jumping mechanism.

Researchers are increasingly finding creative uses for origami in engineering applications. Origami has been used in kinetic architectures [30] and self-folding robots [31], as well as in surgical devices [32] and DNA devices [33]. Origami has also been investigated due to its unique mechanical properties deriving from specific folding patterns, such as tunable nonlinear stiffness resulting in negative and quasi-zero stiffness [34, 35] and multi-stability [36, 37]. In this paper, we investigate the feasibility of using origami as the energy storage mechanism in an attempt to generate the desired "strain-softening" effect for improved dynamic performance. We use a modified version of the Tachi-Miura polyhedron (TMP) [38] origami structure as the basis for the energy storage device. A theoretical model for the force-displacement curve [38] is used to generate a dynamic model in which two end-point masses are secured to either end of the origami bellow, simulating a jumping mechanism. The dynamic performance of the TMP jumping mechanism is analyzed based on the air-time and clearance of the structure, and the geometric parameters of the TMP are optimized to improve the dynamics of the jumper. We also use a creasing technique known as plastically annealed lamina emergent origami (PALEO) [39] to shrink the hysteresis loop observed during a compression cycle in order to increase the efficiency of the TMP structure. In addition to the optimized TMP jumper, another jumper exhibiting a linear force-displacement curve is fabricated in order to serve

2

as a jumper with a representative linear spring, and the dynamic performance of both designs are compared to one another.

Chapter 2

Using Origami Folding to Generate the Desired Strain-Softening Behavior

2.1 Deriving Force-Displacement Relationship of TMP Bellow with Stiffness Modifications

In this study, a modified Tachi-Miura Polyhedron (TMP) origami folding technique is used to achieve a force-displacement curve with the desired strain-softening effect. The TMP is a type of rigid-foldable origami structure consisting of main-folds, which are parallel to the ground, and sub-folds, which are creased at an angle to the main folds. The term *rigid foldable* is used to describe a type of origami in which the facets are rigid and do not undergo deformation during folding process [38], [40]. This assumption implies that the folding behavior of the structure can be described entirely by the rotation of the main-folds and the sub-folds. These folds are treated as torsional springs with an assigned stiffness [40]. Using the rigid-foldable assumption in conjunction with the virtual work principle, the force-displacement relation of the TMP can be described in terms of the

crease angles as shown below [38].

$$F = \frac{-32}{d\cos\theta_M} \left[k_M \frac{N-1}{N} \left(\theta_M - \theta_{M_0}\right) + k_S \frac{\cos^3 \frac{\theta_G}{2} \sin\theta_M}{\cos\alpha \sin\theta_S} \left(\theta_S - \theta_{S_0}\right) \right] \qquad (2.1)$$

In Equation (2.1) , N refers to the number of unit cells in the TMP structure, d is the unit cell height, k_M and k_S are the torsional stiffness of the main-folds and the sub-folds, respectively, and α is the angle of the sub-folds relative to the main-folds. θ_M is half the dihedral angle of the main-fold, θ_S is half the dihedral angle between the facets of the sub-folds, and θ_G is the angle between the x-axis and the main fold. θ_{M_0} and θ_{S_0} are the resting main-fold and sub-fold angles, respectively. These parameters are shown in Figure 2.1, and the kinematic relations between the folding angles are presented below. The relationship between the displacement of the structure and the crease angles is shown in Equations (2.2)-(2.6), where u is the displacement of the TMP from its resting height. The stiffness of the main-folds and the sub-folds were measured experimentally on a per-unit-length basis – this procedure is outlined in Section 3.1.2. The per-unit-length stiffness is multiplied by the length of the crease within the unit cell. The equations used to calculate the total stiffness for each crease are show below, where $\hat{k}_M$ and $\hat{k}_S$ are the per-unit-length stiffness of the main-folds and the sub-folds, respectively. The amount that the TMP is compressed during a compression cycle is defined by the folding ratio FR shown in Equation (2.7), which determines the final displacement of the structure through the final main-fold angle θ_{M_f}.
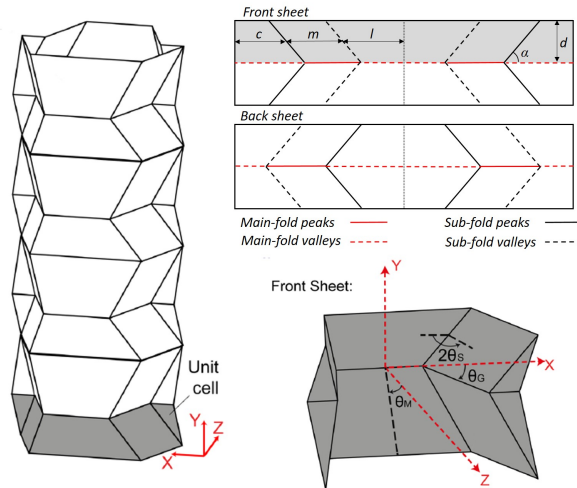
Figure 2.1: TMP bellow with shaded unit cell detailing the geometric parameters as well as folding angles between the facets.

5

$$\theta_M = \sin^{-1}\left(\sin\theta_{M_0} - \frac{u}{Nd}\right) \tag{2.2}$$

$$\theta_G = 2\tan^{-1}\left(\tan\alpha\cos\theta_M\right) \tag{2.3}$$

$$\theta_S = \cos^{-1}\left(\frac{\sin\frac{\theta_G}{2}}{\sin\alpha}\right) \tag{2.4}$$

$$k_M = \hat{k}_M\left(l + m + c\right) \tag{2.5}$$

$$k_S = \hat{k}_S\frac{d}{\sin\alpha} \tag{2.6}$$

$$FR = \frac{90° - \theta_{M_f}}{90°} \tag{2.7}$$

However, the derived reaction force-displacement relationship presented in Equation (2.1) does not consider the deformation limits due to rigid folding. As the creases are compressed toward $\theta_M = \theta_S = 0°$, the facets of the TMP will come into contact with one another, resulting in an increase in the force response. A similar effect occurs when the TMP is extended toward the upper limit of $\theta_M = \theta_S = 90°$ which results in an increased force response when the structure is in tension due to in-plane deformation of the facets. In order to more accurately represent the force-displacement behavior of the TMP, we adopt a method developed by Liu and Paulino [40] to impose a stiffness increase within the main-folds and the sub-folds when these angles exceed pre-defined upper and lower bounds. Through comparison with experimental data, a lower bound of $\theta_1 = 38°$ and an upper bound of $\theta_2 = 70°$ were selected as the pre-defined folding limits. The increase in stiffness is defined in the following equations, where k_{M_0} and k_{S_0} are the unmodified main-fold and sub-fold stiffness.

$$k_M = \begin{cases} k_{M_0}\sec^2\left(\frac{\pi(\theta_M-\theta_1)}{3.5\theta_1}\right), & 0 < \theta_M < \theta_1 \\ k_{M_0}, & \theta_1 \leq \theta_M \leq \theta_2 \\ k_{M_0}\sec^2\left(\frac{\pi(\theta_M-\theta_2)}{2\pi-3.5\theta_2}\right), & \theta_2 < \theta_M < \pi \end{cases} \tag{2.8}$$

$$k_S = \begin{cases} k_{S_0}\sec^2\left(\frac{\pi(\theta_S-\theta_1)}{3.5\theta_1}\right), & 0 < \theta_S < \theta_1 \\ k_{S_0}, & \theta_1 \leq \theta_S \leq \theta_2 \\ k_{S_0}\sec^2\left(\frac{\pi(\theta_S-\theta_2)}{2\pi-3.5\theta_2}\right), & \theta_2 < \theta_S < \pi \end{cases} \tag{2.9}$$

Figure 2.2 shows the reaction force-displacement curve of a TMP structure with $c = d = l = m = 30\text{mm}$, $N = 8$, $\alpha = 40°$, and $\hat{k}_M = \hat{k}_S = 0.005\frac{\text{N}}{\text{rad}}$. The effect of the imposed stiffness increase is shown with respect to the main-folds and sub-folds, as well as the total force response.
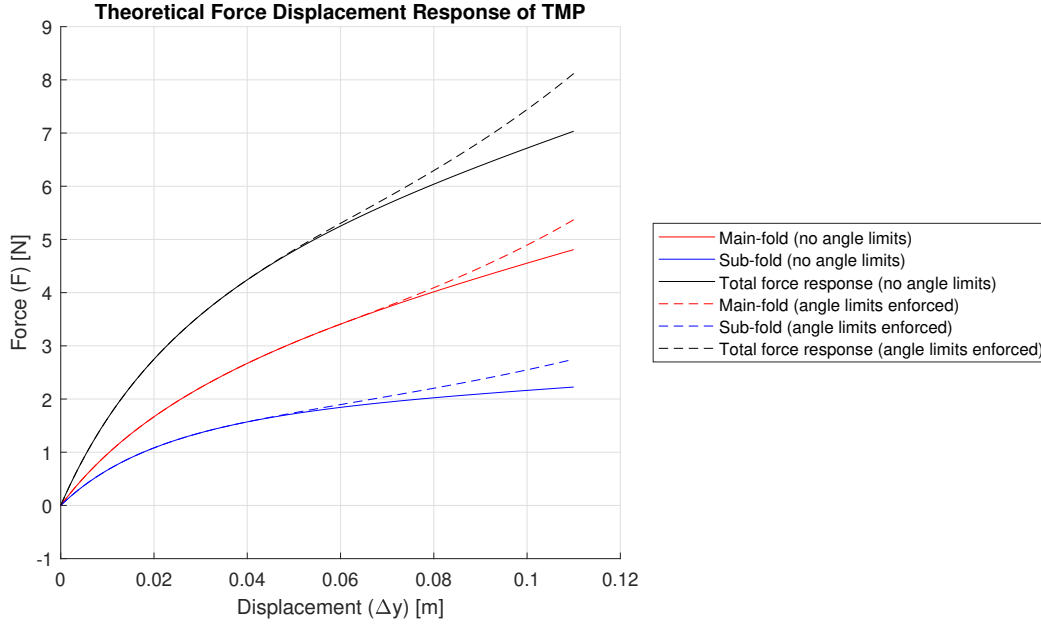
Figure 2.2: Force-displacement response of TMP with and without the stiffness increase at the angle limits

The contributions of the main-folds and sub-folds are separated in order to better understand the reaction force-displacement response of the TMP structure. Although the per-unit-length stiffness of the main-fold and sub-folds are both $0.005\frac{\text{N}}{\text{rad}}$, the main-fold length with these parameters is 90 mm whereas the sub-fold length is 46.6 mm. The greater main-fold crease length results in a larger force response when compared to the sub-folds, indicating that a larger portion of the force response of the TMP structure arises naturally from the main-folds when the stiffness of the main-folds and sub-folds are equal.

However, it is also evident from Figure 2.2 that the response of the sub-folds exhibits a stronger non-linearity than the main-folds. This is a result of the sub-folds resting at an angle to the horizontal axis at the beginning of compression, which stiffens the structure during the early stages of compression. As the TMP moves through compression, the sub-folds become increasingly parallel with the horizontal main-folds, offering less resistance to folding. Conversely, the main-fold response is more linear, which can be explained by the fact that the main-folds remain parallel to the horizontal axis throughout the folding process. Therefore, if greater non-linearity is desired, the per-unit-length stiffness of the sub-folds should be relatively greater than that of the main-folds. On the other hand, if a linear response is desired, the main-folds should have a relatively greater

stiffness than the sub-folds.

2.2   Dynamics of TMP Jumper

The TMP jumping mechanism is shown in Figure 2.3a. Two equivalent masses are secured to either end of the TMP bellow which acts as a nonlinear spring. Additionally, the TMP will impart a damping effect during the jump, which results in a gradual decrease in the amplitude of the oscillations between the endpoint masses. The effect of this energy dissipation is discussed in-depth in Section 3.4. In order to only focus on the effects of nonlinear stiffness on the jumping performance of the origami structure and the optimization of the TMP parameters, we assume that damping is zero.

The jumper is actuated by an external force which compresses the TMP, storing energy for the jump. The jumping process is divided into two separate phases: the pre-jump and post-jump phase. During the pre-jump phase, the external force is suddenly released, allowing the upper mass m_2 to accelerate upward. This phase is complete once the lower mass m_1 leaves the ground. The equation of motion during the pre-jump phase is as follows:

$$m_2 \ddot{y}_2 = F(y_2 - y_1) - m_2 g \tag{2.10}$$

In Equation (2.10) , F is the restorative force provided by the TMP bellow as a function of displacement $(y_2 - y_1)$. The post-jump phase begins as soon as the lower mass m_1 leaves the ground and continues until the jumper returns to the ground. In order for the lower mass to leave the ground, the tensile force within the TMP bellow must exceed the weight of the lower mass $(F > m_1 g)$. The position of each mass is tracked during this phase, resulting in the development of two equations of motion which are shown below:

$$m_1 \ddot{y}_1 = -F(y_2 - y_1) - m_1 g \tag{2.11}$$

$$m_2 \ddot{y}_2 = F(y_2 - y_1) - m_2 g \tag{2.12}$$

Results from the pre-jump phase are used as the initial conditions for the equations of motion

during the post-jump phase. These equations are converted into a system of first order ODEs and solved using *ode45* in MATLAB. Figure 2.3b shows the theoretical time response of a jump where the upper and lower masses are tracked through both the pre-jump and post-jump phase.

(a) Representative spring-damper model of TMP

(b) Jumping performance metrics of dynamic model
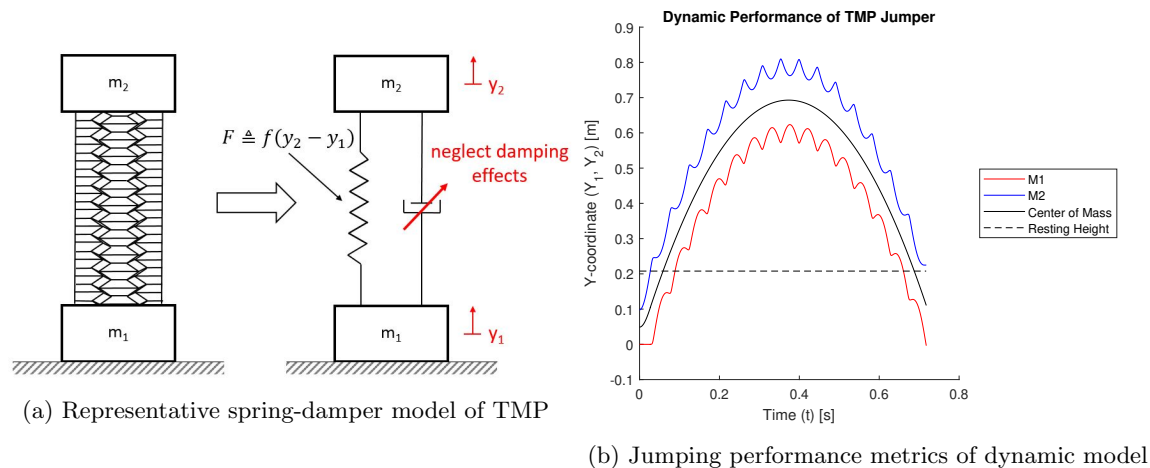
Figure 2.3: Dynamic Model of TMP jumper visualizing the clearance and air-time performance metrics

2.3 Parametric Study of TMP Design Variables

Before an optimization study was conducted on the TMP geometry to optimize the jumping performance of the structure, a parametric study was carried out in order to gain insight into the effect that each design variable has on the force-displacement response, and consequently the dynamic response, of the TMP jumper. To this end, each design variable discussed in Section 2.1 was varied between two pre-defined bounds while all other parameters were held constant. For example, the number of unit cells N was incremented from 6 to 10 while all other parameters were held constant at the mid-point of their bounds.

The lower bound on the number of unit cells ensures that the structure will exhibit proper folding and reduces the impact of undesirable boundary effects due to friction. The upper bound was selected to minimize the possibility of buckling during compression. The bounds on the length parameters d, l, m, and c were chosen to place an upper limit on the geometry of the TMP, and the lower limit ensures that the unit cell has sufficient space between creases for proper folding. The lower bound on the sub-fold angle α was chosen to minimize the possibility of buckling during a

9

Table 2.1: TMP geometry values and bounds used during the parametric study

Constraint Parameters	Bounds During Parameter Sweep
$N = 8$	$6 < N < 10$
$d = 30\text{mm}$	$20\text{mm} < d < 40\text{mm}$
$1 = 30\text{mm}$	$20\text{mm} < 1 < 40\text{mm}$
$m = 30\text{mm}$	$20\text{mm} < m < 40\text{mm}$
$c = 30\text{mm}$	$20\text{mm} < c < 40\text{mm}$
$\alpha = 50°$	$30° < \alpha < 70°$

compression cycle due to a narrow footprint, and the upper bound was chosen to ensure that the TMP is still capable of folding properly.

The resulting force-displacement response was observed for each parameter sweep, where the structure was compressed to a folding ratio of 0.75 for each trial. Table 2.1 lists the upper and lower bounds for each design variable, as well as the constant value of each parameter during the sweep, and Figure 2.4 shows the theoretical force-displacement response as each parameter moves through its respective range.

When examining the effect of each parameter on the force-displacement response of the TMP structure, it is important to note that in each trial, the final displacement was defined by a folding ratio of 0.75. In anticipation of experimental study, the folding ratio was used to determine the final displacement of the structure in an attempt to keep the crease deformation within the elastic range. In other words, if the final displacement was directly defined and held constant for each trial, the creases would undergo plastic deformation when the parameters that affect the structure height (N and d) are small because the TMP would undergo the same displacement while having a shorter height.

From Figure 2.4 it is immediately evident that some parameters have a far more drastic influence on the force-displacement response of the structure than others. The main-fold lengths l, m, and c have very little impact on the shape of the force-displacement curve, which is a result of the linear contribution of the main-folds in the overall stiffness of the structure as discussed in Section 2.1. As the length of the main-folds increase, the contribution to the total force response also increases due to the relationship between the crease stiffness k_M and the main-fold lengths as shown in Equation (2.5).

(a) Variation of N

(b) Variation of d

(c) Variation of l

(d) Variation of m

(e) Variation of c

(f) Variation of α
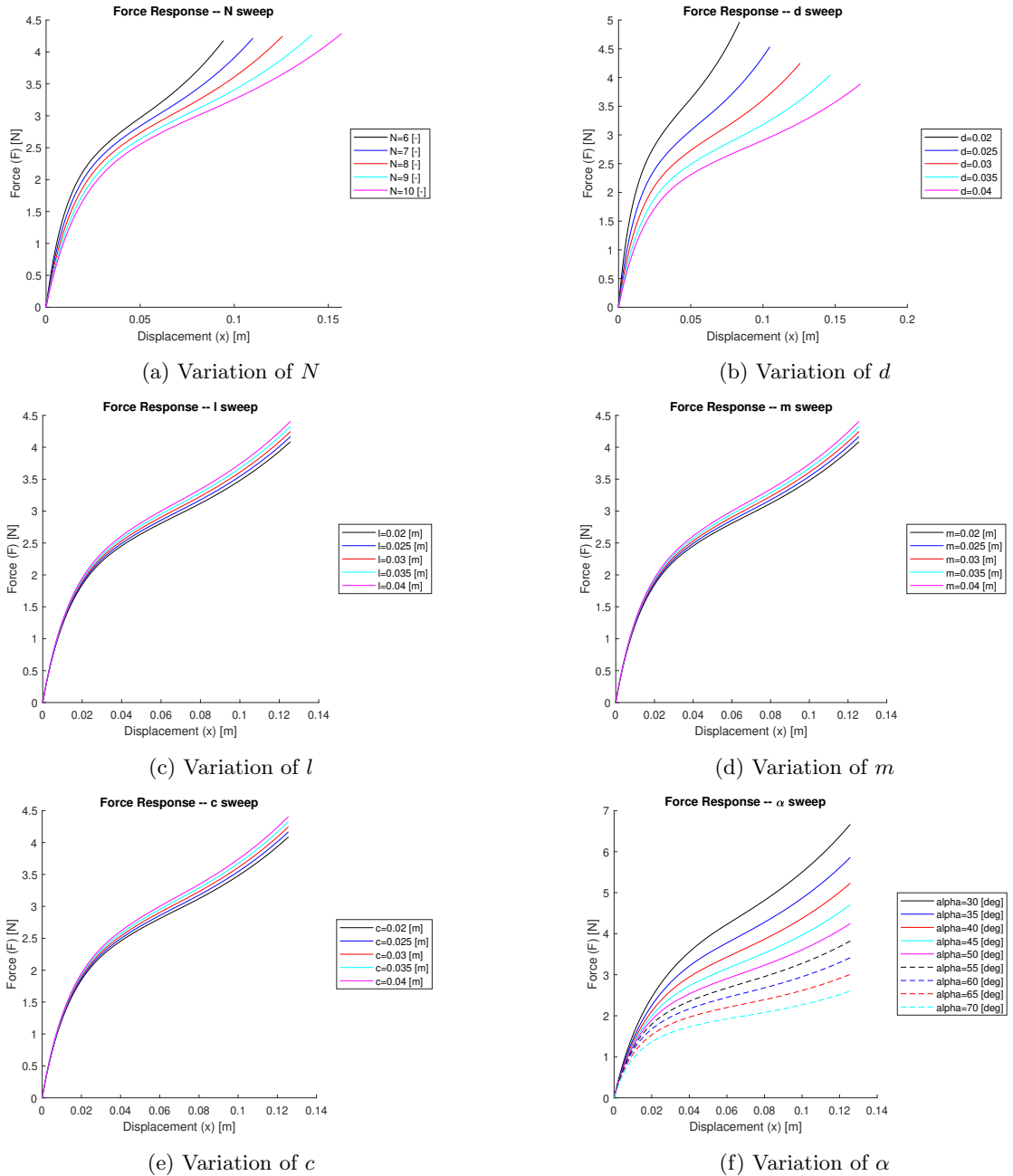
Figure 2.4: Parametric study of TMP design variables

The number of unit cells N has only a very slight effect on the final magnitude of the force response, but a smaller number of unit cells seems to increase the stiffness of the structure in the early stages of folding. Alternatively, a larger number of unit cells allows the structure to undergo greater displacement before reaching the folding ratio limit (and subsequent plastic deformation). Therefore, a larger number of unit cells would allow the structure to store more energy through compression.

Similar to the number of unit cells, the unit cell height is also used to define the total height of the TMP structure. Therefore, as the unit cell height decreases, the final displacement of the structure will decrease as well to prevent the creases from undergoing plastic deformation. Unlike N, however, we notice a dramatic increase in the force response for smaller values of d. It is more difficult to predict what the optimal value of this parameter would be – a larger unit cell height would allow for a greater displacement of the overall structure before plastic deformation of the creases, but a smaller value would result in a stronger force-displacement response. It is reasonable to expect the unit cell height to trend as low as possible while still allowing the creases to remain in the elastic deformation range to maximize energy retention during extension.

The angle of the sub-folds α has a clear preference toward lower values when considering the amount of energy stored, which is a result of the increased non-linear contribution of the sub-folds as discussed in Section 2.1. Additionally, this parameter is not affected by the folding ratio, which is dependent only on the main fold angle θ_M.

2.4 Multi-Objective Optimization to Improve Dynamic Performance

The TMP bellow was optimized to enhance the dynamic performance of the jumper using a non-dominated sorting genetic algorithm (NSGA-II), which is a multi-objective evolutionary algorithm (MOEA). The NSGA-II generational algorithm was selected due to it's ability to quickly converge to a solution while preserving diversity in the population [41]. The non-dominated sorting is achieved using a domination count n_p which represents the number of solutions that dominate the solution p, as well as a set of solutions S_p which are dominated by the solution p. Preservation of diversity is achieved through the use of a density function which measures the distance between individuals in a population and through the use of a crowd-comparison operator which guides the

selection of individuals toward a more uniformly distributed Pareto front [41]. These traits are desirable in an MOEA because a diversified Pareto front ensures that a wide variety of possible solutions have been considered, leading to the best possible solution. A population of 100 random individuals was used as the initial parameter set, and the NSGA-II algorithm moved through a total of 2500 individuals during the optimization.

Table 2.2: Parameter bounds imposed during optimization

Parameter Bounds	
$6 < N < 10$	$30° < \alpha < 70°$
$20\text{mm} < d < 40\text{mm}$	$20\text{mm} < 1 < 40\text{mm}$
$20\text{mm} < m < 40\text{mm}$	$20\text{mm} < c < 40\text{mm}$

Table 2.3: Additional variables required for dynamic simulation

Additional Optimization Variables	
End Masses:	$m_1 = m_2 = 0.02$ kg
Resting Main-Fold Angle:	$\theta_{M_0} = 60°$
Folding Ratio:	$FR = \frac{90° - \theta_{M_f}}{90°} = 0.75$
Main-Fold Stiffness:	$\hat{k}_M = 0.0186\frac{\text{N}}{\text{rad}}$
Sub-Fold Stiffness:	$\hat{k}_S = 0.0946\frac{\text{N}}{\text{rad}}$

$$2l - d\cot\alpha + 2m\cos\alpha \geq 0 \tag{2.13}$$

$$\frac{d}{2\tan\alpha} - l \leq -0.01 \text{ m} \tag{2.14}$$

The optimization software ModeFRONTIER was coupled with MATLAB, where the ODE solver *ode45* was used to solve equations (2.10), (2.11), and (2.12). The two objectives used in the NSGA-II algorithm were the air-time and clearance achieved by the jumper. Air-time is the difference between the landing and take-off time, and clearance is the maximum height achieved by the lower mass m_1. In the multi-objective optimization problem, both the air-time and clearance were maximized in an effort to optimize the dynamic performance of the jumper.

The upper and lower bounds on each parameter are listed in Table 2.2 and were identical to the bounds used in the parametric study. Two constraints are imposed for the optimization problem. The first constraint ensures that there are not conflicting crease lines in the design of the TMP geometry, shown in Equation (2.13). The second constraint defines a minimum main-fold length to ensure ease of fabrication and folding, shown in Equation (2.14). Table 2.3 lists additional design specifications for the optimization of the TMP. These specifications are required for use in the dynamic simulation and include the masses at each end of the TMP jumper, the resting main-fold angle, the folding ratio, and the main- and sub-fold stiffness on a per-unit-length basis. The crease stiffness values were found experimentally, the procedure for which is outlined in Section 3.1.2.
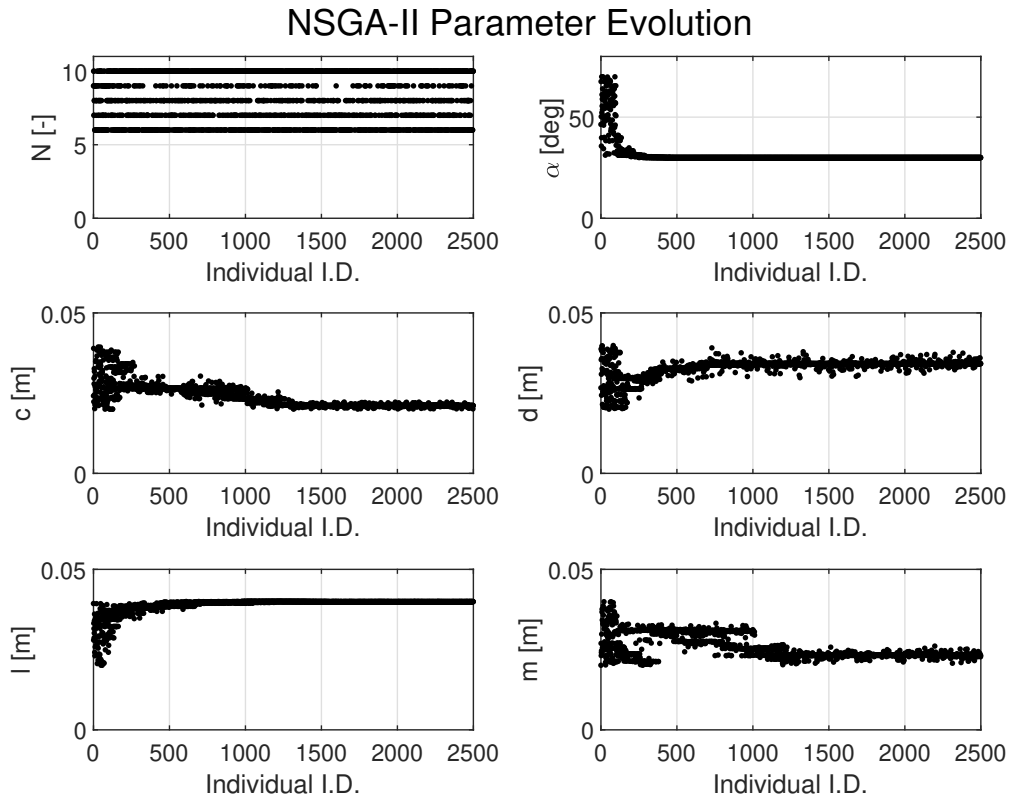
NSGA-II Parameter Evolution

Figure 2.5: Evolution of design parameters during NSGA-II optimization

The results of the optimization are shown in Figure 2.5, where the convergence of each parameter is shown over the course of the 2500 function evaluations. Although difficult to observe given the large number of individuals on the plot, the number of unit cells N trends toward the upper

bound of 10. The convergence of this parameter is not as strong as the other design parameters, but it is still evident when examining the density of the individuals at each parameter value ($6 \leq N \leq 10$). This convergence trend agrees with the preliminary results of the parametric study discussed in the previous section – as the number of unit cells increases, the TMP bellow is able to move through a greater displacement before experiencing plastic deformation at the creases, thus allowing for greater energy storage. The sub-fold angle α converges very rapidly to its lower bound of 30°, which also agrees with the parametric study. As this angle is decreased, the contribution of the sub-folds to the overall force response is increased and we achieve the desired strain-softening effect required to store more of energy.

The length parameters (c, d, l, m) define the size of the TMP unit cell, and therefore have a direct effect on the overall mass of the structure. This is an important relationship to consider when examining the trade-offs between increasing the crease length (and subsequent force-response) at the cost of decreasing the dynamic performance of the TMP jumper due to the increased mass. The main-fold lengths c and m both converge to small values near the lower bound of 0.02 m, while the third main-fold length l converged to the upper bound of 0.04 m. From the parametric study in Section 2.3, the effect of the unit cell height d was difficult to predict due to the unique trade-offs corresponding to this design parameter. A larger unit cell height allows for greater displacement and subsequent energy storage, but a smaller unit cell height resulted in an increased force-response. It should also be noted that the dynamic performance of the jumper was not considered in Section 2.3 – only the force-displacement response was examined. Therefore, it is understandable that the optimal value of this design parameter is somewhere in the middle of its bounds.

Table 2.4: Parameter sets corresponding to the optimal dynamic solution

Maximum Objective Value		TMP Parameters					
		N [-]	α [°]	c [mm]	d [mm]	l [mm]	m [mm]
Air-time	0.519 s	10	30	21.1	34.2	39.9	23.2
Clearance	359.7 mm	10	30	21.1	34.2	39.9	23.2

The results of the optimization are detailed in Table 2.4. Although a multi-objective optimization was conducted and a Pareto front exists, the difference between the parameters that maximize each objective was negligible, so a single optimal solution set is used to design the opti-

15

mized nonlinear TMP which maximizes both air-time and clearance.

2.5   Design of Linear TMP

Sadeghi *et. al.* [21] demonstrated the theoretical benefits of a nonlinear elastic element when compared to a linear element for use in a jumping mechanism. In an effort to experimentally validate these results, a TMP with a set of design variables different than the optimized nonlinear TMP was designed such that it exhibited a linear force-displacement response. TMP origami was chosen for the linear spring in order to preserve consistency between the nonlinear and linear jumpers.

The design parameters of the linear TMP were determined through the use of the Simplex and Powell single objective optimization algorithms in ModeFRONTIER. Two different algorithms were used as a way to cross-validate the results of the optimization across both methods. The upper and lower bounds placed on the design variables were consistent with those used in the nonlinear optimization shown in Table 2.2. The final displacement of the linear structure was constrained to be equal to the final displacement of the nonlinear structure, allowing for a more direct comparison of the force-displacement responses between both structures. In order to design a linear TMP structure, a penalty was imposed for deviation from a linear response. An ideal linear force-displacement curve is defined as a perfectly linear response with the same final force and displacement values as the non-linear TMP, and the total error between the linear TMP and the ideal linear curve is minimized. This is summarized in the objective function shown in Equation (2.15). The error between the two curves was sampled at each point within the discretized displacement (roughly 2,000 sample points), and the sum of these errors was used as the objective function to fit the TMP response to the ideal linear curve.

$$\textbf{Minimize: } \text{Error} = \sum \mid F_{TMP} - F_{ideal} \mid \tag{2.15}$$

Table 2.5: Linear TMP parameter sets resulting from single objective optimization

	Design Variables						
	N [-]	α [°]	c [mm]	d [mm]	l [mm]	m [mm]	Error [N]
Powell	8	70	34.0	21.6	31.7	39.1	205.1
Simplex	8	70	39.6	21.1	20.0	40.0	206.5

Table 2.5 shows the linear parameters sets resulting from the optimization using both Powell and Simplex algorithms. Both methods yield similar magnitudes of error, but the Powell algorithm converged to a parameter set that offers slightly better agreement between the TMP and ideal linear spring. In addition to the TMP parameters, the linear design included adjustment of the main-fold and the sub-fold stiffness. From Section 2.1, the nonlinearity of the force-displacement response arises from the contributions of the sub-folds. This characteristic is exploited in the nonlinear TMP design by intentionally stiffening the sub-folds and weakening the main-folds as shown by the crease stiffness in Table 2.3. Conversely, the linear TMP was designed with weak sub-folds ($\hat{k}_S = 0.0186\frac{\text{N}}{\text{rad}}$) and stiff main-folds ($\hat{k}_M = 0.0946\frac{\text{N}}{\text{rad}}$).

Chapter 3

Experimental Study

3.1   Energy Loss and Hysteresis Problem

The primary challenge in utilizing origami as a mechanism for energy storage is minimizing energy loss during a compression cycle. Specifically, maintaining energy storage during the extension phase is critical for jumping applications in order to maximize the dynamic performance of the mechanism. We define the energy efficiency of the TMP structure as the ratio of the energy released during extension to the energy stored during compression as shown in Equation (3.1). This metric is used to quantify the amount of hysteresis observed in the TMP during a compression cycle.

$$\eta = \frac{E_{expansion}}{E_{compression}} \tag{3.1}$$

Compression cycles were conducted using an ADMET MTESTQuattro tensile tester to collect force-displacement data for the TMP bellow. The MTESTQuattro uses powder-coated steel plates to compress the sample while a 25 lb load cell collects force data. Friction between the endpoints of the TMP and the steel plates of the tensile tester was identified as a potential source of hysteresis. Additionally, plastic deformation at the creases of the TMP was also investigated as a source of energy loss. The following sections outline the steps taken to address both sources of hysteresis.

3.1.1 Hysteresis Due to Friction

Energy loss due to friction was reduced through the use of low-friction polytetrafluoroethylene (PTFE) sheets, known commercially as Teflon. PTFE is well known for its use in low-friction applications with a coefficient of kinetic friction of roughly 0.3. A sample TMP bellow fabricated from polypropylene was compressed to a folding ratio of 0.75 at varying deformation rates.

Table 3.1: Effect of PTFE sheets on efficiency during a TMP compression cycle

	Deformation Rate $[\frac{mm}{s}]$	Efficiency [-]	Average Efficiency [-]	Standard Deviation [-]
Bare Steel	4	0.690		
	6	0.696	0.699	0.0086
	8	0.700		
	10	0.708		
PTFE Sheets	4	0.704		
	6	0.709	0.713	0.0084
	8	0.719		
	10	0.722		

A comparison between the efficiencies with and without the PTFE sheets is detailed in Table 3.1, which reveals an increase in average efficiency of roughly 1.5% with the introduction of the low-friction PTFE. Although marginal, this reduction in hysteresis was still considered beneficial for the purposes of the jumping mechanism application, and PTFE sheets were used in all subsequent quasi-static and dynamic experiments. Compression cycles were conducted at different deformation rates in order to understand the impact of this testing parameter on the efficiency of the TMP structure to inform future trials. However, the standard deviation in efficiencies across the range of deformation rates was 0.86% and 0.84% for the bare steel and PTFE trials, respectively, indicating the deformation rate has a relatively low impact on the hysteresis of the structure.

3.1.2 Hysteresis Due to Plastic Deformation at the Creases

In classic origami, creases are created by concentrating the deformation of the material along a line, which then holds its shape – this methodology inherently exhibits plastic deformation and is not conducive to a "springy" response. A type of creasing technique known as plastically annealed lamina emergent origami (PALEO) was examined for its use in energy retention to further reduce hysteresis. PALEO works by folding the material into its desired state – often plastically deforming
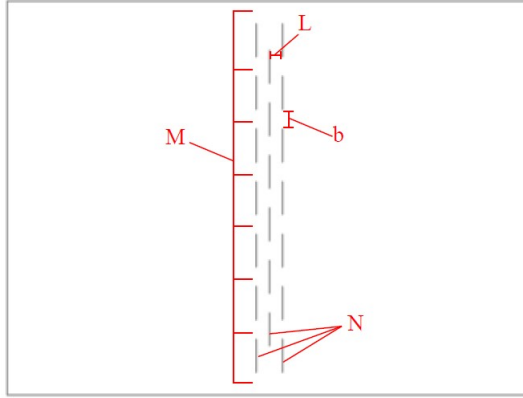
Figure 3.1: Sample cut pattern for PALEO crease detailing PALEO crease parameters

the material – at which point the polymer is annealed well above the glass transition temperature to relax the internal stresses [39]. This leaves the creases in a tension-free state and increases the elastic folding range of the crease, thus minimizing hysteresis due to plastic deformation. In addition to the annealing process, PALEO creases are designed with a series of cuts parallel to the crease. An example cut configuration is shown in Figure 3.1. The number of columns is denoted as N, the number of 'hinges' (material between cuts) is denoted as M, the spacing between the cuts is denoted as b, and the spacing between the columns is denoted as L. From 2.1, the nonlinearity of the force-displacement profile exhibited by the TMP arises from contributions from the sub-folds. Therefore, the objective of the PALEO crease study is to determine how the cut configuration influences the stiffness of the crease, allowing for the design of a TMP bellow with stiff sub-folds and weak main-folds to maximize the strain-softening effects for increased energy storage.

A series of PALEO cut configuration samples were cut on an Epilog Fusion M2 laser cutter, folded to their fully-folded state, and annealed at 170°C for 60 minutes. This procedure was used based on results from Sargent et. al. [42], as 170°C was the mid-point of the temperature range which showed the best performance in terms of the force response of the PET crease. Results from [42] also indicate that rapid cooling of 15°C/min from annealing temperature to glass transition temperature, followed by slow cooling of 0.5°C/min from glass transition temperature to room temperature should be used to achieve the best results in terms of energy retention of the crease.

In order to investigate how these cut parameters effect the stiffness of the PALEO crease, a series of sixteen different crease configurations were fabricated using an Epilog Fusion M2 laser cutter. The designs are shown in Figure 3.2. The samples were folded completely such that the facets

were in contact, then placed into a frame at a 90° fold angle for annealing. After annealing, the facets on either side of the crease were reinforced with a 1.5 mm thick section of polypropylene in order to prevent deformation of the facets during testing. The stiffness of each crease was measured by applying a load to the endpoint of the rigid facet and observing the angular deflection of the crease. A visual representation of the experimental setup is shown in Figure 3.3. Each PALEO sample was clamped in a vice before being subjected to a load applied at the endpoint of the free facet. Four measurements were taken at increasing loads in order to understand how the stiffness changes through the folding angle from 90° to roughly 30°. Torsional stiffness was calculated using Equation (3.2), where $F_\perp$ is the perpendicular component of the applied load, $d_\perp$ is the perpendicular distance from the hinge to the applied load, and θ_0 and θ_l and the resting and loaded angle, respectively. The results of the stiffness study are plotted in Figure 3.4.

$$k_\theta = \frac{F_\perp d_\perp}{\theta_0 - \theta_l} \tag{3.2}$$
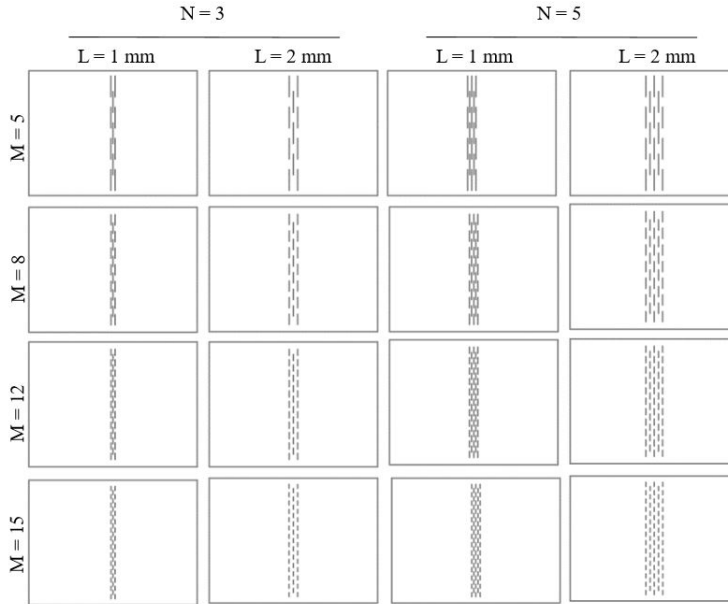

Figure 3.2: PALEO cut configurations used in crease stiffness study

From Figure 3.4, the torsional stiffness is relatively small near the resting angle $\theta_{disp} = 0°$ but quickly increases as the angular displacement increases. These results support the assumption

21
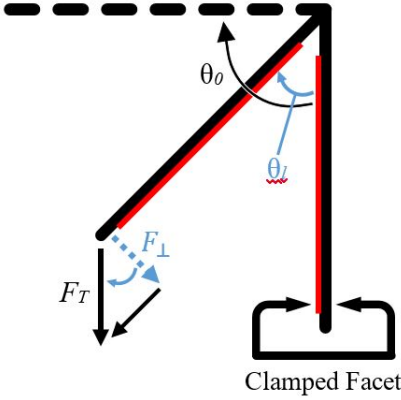
Figure 3.3: Testing schematic for PALEO creases illustrating loading methodology

Table 3.2: Selection of PALEO crease configurations

	M [-]	N[-]	L [mm]	b [mm]	Torsional stiffness of sample (k_θ) [$\frac{Nm}{rad}$]	Torsional stiffness per-unit-length ($\hat{k}_\theta$) [$\frac{N}{rad}$]
Weak fold configuration	5	5	1	5	0.0011	0.0186
Stiff fold configuration	15	3	2	2	0.0057	0.0946

that the crease stiffness should be inflated as the facets become closer together with increasing angular displacement as shown in Equations (2.8) and (2.9). The crease configurations selected for the stiff and weak creases are summarized in Table 3.2, along with the corresponding per-unit-length torsional stiffness which is calculated by dividing the stiffness of the sample by the crease length of the sample. The weak PALEO configuration was integrated into the main-folds of the optimized nonlinear TMP design, and the stiff PALEO configuration was integrated into the sub-folds of the nonlinear TMP design.

Two TMP structures with identical geometric design parameters were fabricated from PET sheets using different creasing methods. PET was selected based on its performance in conjunction with PALEO techniques from Klett [39], who used 125 μm thick sheets. The control TMP structure was fabricated using a Graphtec FCX4000 cutting table. The creases were scored into the PET sheets at a depth of 60 μm, or just under half the sheet thickness. The creases of the control TMP will hereby be referred to as *standard cut* creases. The second TMP utilized the results of the PALEO crease study listed in Table 3.2 to incorporate the stiff PALEO crease into the sub-folds
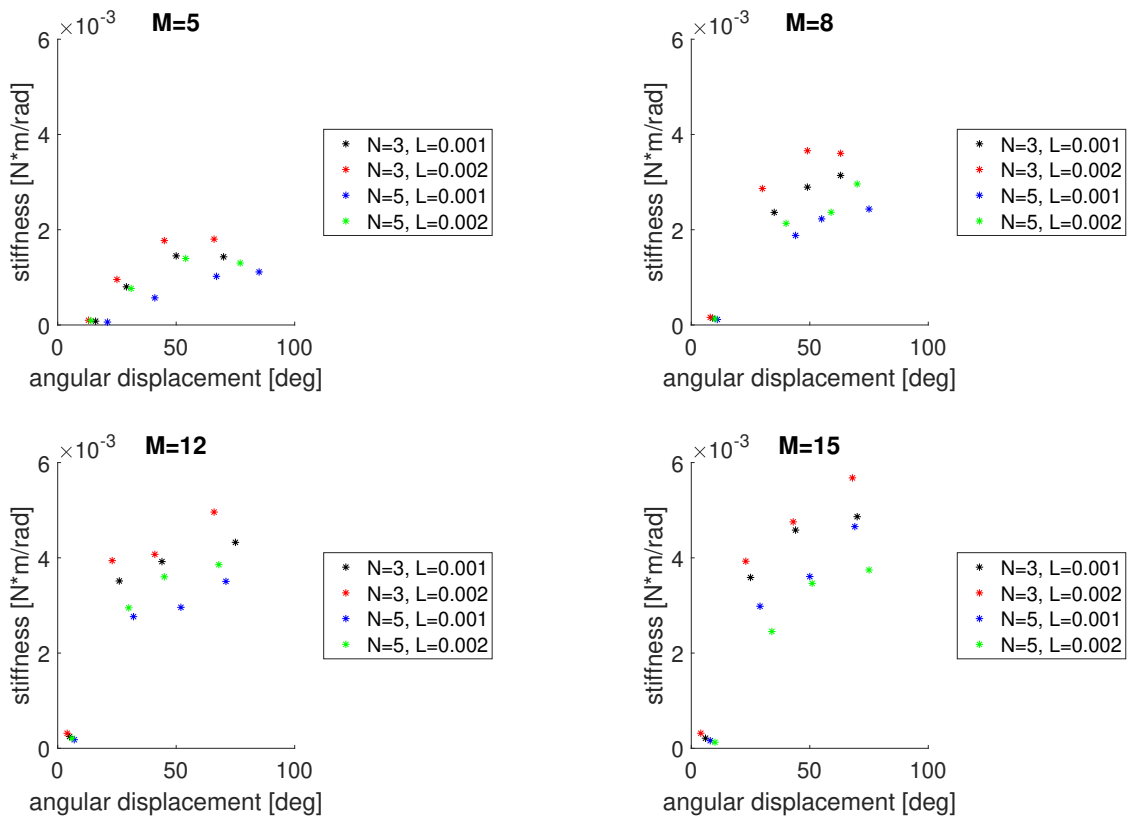
Figure 3.4: Stiffness of PALEO crease configurations, categorized by the hinge length M. Additional crease parameters are denoted in the legend of each plot.

and the weak PALEO crease into the main-folds to exaggerate the strain-softening behavior of the TMP. The crease designs are shown in Figure 3.5. Both structures were annealed in-shape and compressed to 110 mm, 130 mm, and 150 mm in a progressive manner to determine if hysteresis became more prevalent as the final displacement was increased. Each displacement trial was repeated five times to ensure consistent results. The force-displacement response is shown in Figure 3.6 and the performance metrics are listed in Table 3.3.
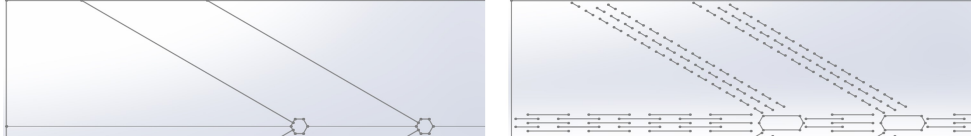
Figure 3.5: TMP crease designs using standard cut and PALEO creases

Table 3.3: Hysteresis results of standard cut creases vs PALEO creases

	Displacement from Resting Height (d) [mm]	Energy Efficiency (η) [-]	Nonlinear to Linear Ratio [-]
Standard Cut Creases	110	0.649	0.828
	130	0.687	0.888
	150	0.639	0.808
PALEO Creases	110	0.878	1.108
	130	0.787	1.029
	150	0.784	0.910

Table 3.3 lists the amount of hysteresis observed during the compression cycles in the form of energy efficiency. Using this metric, it becomes evident that the PALEO creases are far more efficient than the standard cut creases, with the PALEO creases outperforming the standard cut creases by as much as 22% efficiency in the 110 mm displacement test. These results are to be expected due to the greater amount of plastic deformation occurring within the standard cut creases. Both crease types exhibit a reduction in efficiency as the maximum displacement is increased, which is a result of an increase in the plastic deformation experienced at the creases as the structure is compressed further.

Another metric used to quantify the performance of the TMP bellow is a ratio between
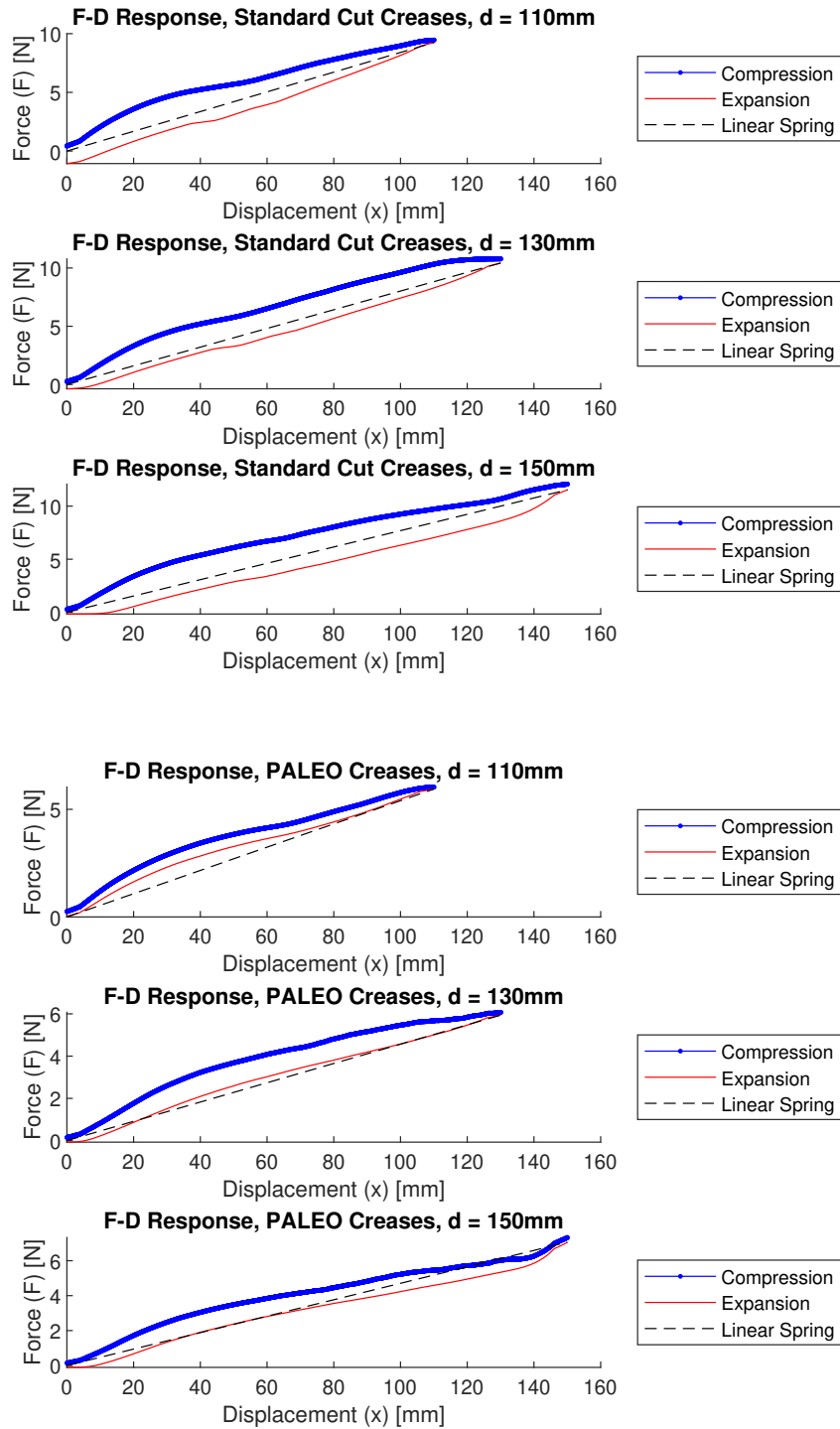
Figure 3.6: Comparison between standard cut creases and PALEO creases for compression cycles at varying displacements.

energy released from the TMP structure during expansion to the energy released from an ideal linear spring, which is labeled as the nonlinear-to-linear ratio in Table 3.3. The ratios of the standard cut creases are significant due to the fact that the TMP geometry has already been optimized for greater energy storage than a linear spring – despite the optimized TMP geometry, the structure will fail to outperform a normal linear spring if the hysteresis problem is not addressed. Here, the plastic deformation at the creases result in enough energy loss that the TMP structure releases less energy than a linear spring at all tested displacements.

Conversely, the cuts incorporated into the PALEO creases result in an increase in the bend radius which reduce the amount of energy loss due to plastic deformation. The greater efficiency of the PALEO creases enables the optimized TMP geometry to outperform the linear spring when releasing energy during expansion. However, these benefits become less evident as the displacement is increased, as shown by the ratio of 0.91 at 150 mm displacement Therefore, a displacement of 110 mm was selected for subsequent dynamic experiments in an effort to maximize the benefits of the nonlinearity of the TMP structure.

3.2   Quasi-Static Force-Displacement Response

Both the nonlinear and linear TMP structures designed in Sections 2.4 and 2.5, respectively were fabricated and tested using the methods discussed in Sections 3.1.1 and 3.1.2. The creases were designed using the PALEO methodology with the stiff and weak crease configurations applied to the appropriate folds: stiff sub-folds and weak main-folds for the nonlinear TMP, stiff main-folds and weak sub-folds for the linear TMP. However, the nonlinear and linear optimized TMP parameters resulted in difficulties during experimental testing.

In the nonlinear TMP, the low sub-fold angle $\alpha = 30°$ resulted in a very thin footprint for the TMP structure when the front and back sheets were assembled. This small footprint coupled with a large number of unit cells ($N = 10$) resulted in significant buckling during initial compression tests. After trial and error, a solution was found by reducing the number of unit cells to $N = 8$, thus reducing the structure height and allowing for reliable compression cycles without buckling.

In the linear TMP design, the large sub-fold angle $\alpha = 70°$ also produced difficulties in acquiring quality compression cycle data. This large angle resulted in undesirable compression behavior in which the structure buckled rapidly cell-by-cell, generating an inconsistent force response.

Through trial and error, the sub-fold angle was lowered until smooth compression cycles could be consistently achieved. The sub-fold angle for the linear TMP was modified to $\alpha = 50°$. Additionally, the number of unit cells was also lowered to $N = 8$ for the linear TMP due to the same buckling issues experienced with the nonlinear TMP. A summary of the revised TMP design parameters is shown in Table 3.4 below.

Both structures were placed in the MTESTQuattro tensile tester and subjected to five compression cycles with a final displacement of 110 mm. The extension phase of the compression cycle for both TMP structures is plotted below as an average of the five trials. Additionally, the theoretical response is plotted for both structures in order to examine the agreement between theoretical and experimental results.

Table 3.4: Revised TMP parameters and crease stiffness for nonlinear and linear configurations

	TMP Parameters					Crease Stiffness	
	N [-]	α [°]	c [mm]	d [mm]	l [mm]	m [mm]	$\hat{k}_M$ [N/rad]	$\hat{k}_S$ [N/rad]
Nonlinear	8	30	21.1	34.2	39.9	23.2	0.0186	0.0946
Linear	8	50	34.0	21.6	31.7	39.1	0.0946	0.0186

Table 3.5: Performance metrics for nonlinear and linear TMP structures

	Experimental Energy [Nm]	Energy Ratio to Ideal Linear Spring [-]	% Error in Energy	Actuation Ratio [-]
Nonlinear	3.63e-4	1.12	2.77%	35.2
Linear	3.34e-4	1.02	11.34%	50.9

When examining the performance of both TMP structures, the most important metric is the amount of energy released by the structure during the extension phase of the compression cycle. This quantity directly relates to the ability of the structure to generate an explosive jump when used as a jumping mechanism. The table below lists performance metrics surrounding the energy capabilities of both structures.

The energy ratio to an ideal linear spring represents a comparison between the TMP structure and a perfect linear spring. For the nonlinear TMP, a ratio greater than one is desirable as this indicates greater energy storage than a standard linear spring. For the linear TMP, this ratio should
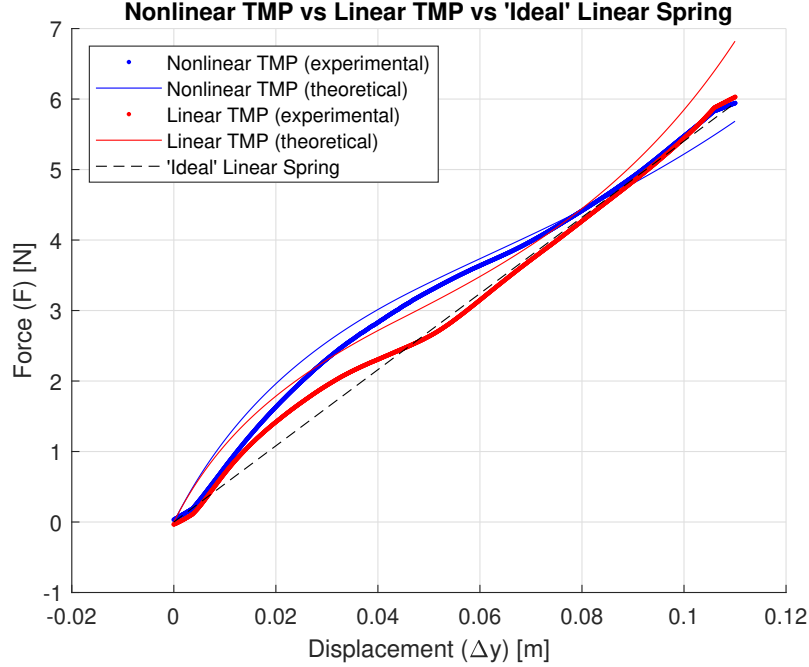
Figure 3.7: Theoretical and experimental force-displacement plots of nonlinear and linear TMP compared to an ideal linear spring

be as close to one as possible, indicating the linear TMP is a good representation of an ideal linear spring. The percent error between the theoretical and experimental results indicates the quality of agreement between the force-displacement model described in Section 2.1 and the experimental results. The model has very good agreement with the nonlinear TMP at 2.77% error, while the linear TMP shows acceptable agreement at 11.34% error. The effect of the error in the approximation of energy storage will be discussed when examining agreement between dynamic experiment and the dynamic model in Section 3.4. From Table 3.5, we see greater experimental energy storage in the nonlinear TMP than in the linear TMP, as well as a greater energy ratio to an ideal linear spring. The linear TMP exhibits a ratio to an ideal linear spring of 1.02, indicating an acceptable representation of a linear spring for use in dynamic tests.

The final column of Table 3.5 lists a ratio comparing the value of the actuating force at the structural limit of the TMP and the weight of the PET sheets used to fabricate the TMP. This is mathematically expressed as follows: $F_{ratio} = \frac{f_{max}}{W_{TMP}}$. The purpose of this metric is to demonstrate the relative strength of these structures. The configuration of the TMP parameters in conjunction with the annealed strength of PALEO creases allows PET sheets – which have a relatively small

weight – to exhibit a large amount of force at the structural limit. The linear TMP has a weight of 0.12 N, whereas the nonlinear TMP weighs 0.17 N. Therefore, because both structures have a very similar maximum force response (f_{max}), the actuation ratio is far greater for the linear TMP due to its lower weight.

3.3   Dynamic performance of the TMP Jumpers

In order to accurately simulate end-point masses on the TMP structure for dynamic testing, steel shim stock was cut to size and adhered to the facets of the top and bottom unit cells of the structure using double-sided tape. This methodology was chosen because the thin shim stock did not interfere with the folding motion of the TMP. However, the amount of mass

Table 3.6: End-point masses attached to nonlinear and linear TMP jumpers during dynamic experiments

	m_1 [kg]	m_2 [kg]
Nonlinear	0.0177	0.0176
Linear	0.0179	0.0179

applied at each end-point was limited by the available facet area on the unit cell. An additional challenge involved equating the masses on both the nonlinear and linear jumpers. Equal masses across both structures allows for direct comparison between the jumping performance of the nonlinear and linear jumpers, but differences in geometry between the structures prevented the exact same sets of masses to be used for both jumpers. A water jet was used to cut the mass designs from the steel shim stock, and the masses applied at each end-point are shown in Table 3.6.

Dynamic data was collected by capturing video footage of each jump at 240 frames per second and moving frame-by-frame to extract take-off time, landing time, and maximum clearance of the lower mass. The jumpers were placed in front of 1-inch square grid paper, providing a height reference for clearance data. Actuation was performed using two segments of thread secured to the jumping platform just behind the TMP. These segments were draped over the TMP and pulled down, compressing the TMP to a displacement of 0.110 m. The threads were then simultaneously cut, allowing the jumper to instantly extend and jump from the platform. This process was repeated ten times for both the nonlinear and linear TMP jumpers, and air-time and clearance data was averaged across the ten trials. Still frames taken from a jump are shown in Figure 3.8 for the nonlinear and linear TMP jumpers. The air-time was measured as the difference between the time stamp on the

landing frame (Figure 3.8g) and the take-off frame (Figure 3.8c), and the clearance was measured using the reference grid as shown in Figure 3.8e.

Table 3.7: Air-time and clearance averages across ten jump trials for both jumper configurations

	Nonlinear		Linear	
	Average	Standard Deviation	Average	Standard Deviation
Air-time [s]	0.461 s	0.014 s	0.0423 s	0.011 s
Clearance [mm]	259.7 mm	14.3 mm	230.6 mm	14.0 mm

Table 3.8: Comparison between optimized nonlinear TMP and linear TMP jumpers

	Nonlinear	Linear	Percent Improvement
Air-time [s]	0.461 s	0.423 s	8.98%
Clearance [mm]	259.7 mm	230.6 mm	12.62%

Table 3.7 shows the dynamic data averaged across ten jump trials for both TMP configurations, and the standard deviation was also calculated to observe the extent of variation across the trials. Both TMP configurations show consistent performance throughout the dynamic experiments, with the air-time metric showing standard deviations of 0.014 s and 0.011 s for the nonlinear and linear jumpers, respectively and the clearance metric showing standard deviations of 14.3 mm and 14 mm for the nonlinear and linear jumpers, respectively.

A comparison between the average air-time and clearance achieved by the nonlinear and linear jumper is shown in Table 3.8. The performance of the nonlinear jumper is compared to the linear jumper as a percent improvement, with air-time increasing by roughly 9% and clearance increasing by nearly 13%. Therefore, the hypothesis of this study has been experimentally supported from these dynamic results. We show that a TMP origami bellow can be optimized to exploit the "strain-softening" behavior in an effort to store more energy, thus improving the dynamic performance when compared to a linear elastic element.

3.4 Use of Equivalent Damping Ratio to Correct Dynamic Model

When comparing the experimental dynamic results to the theoretical results predicted from the dynamic model, there exists a large discrepancy between the two sets of data. While the air-

(a) Jump experiment with optimized nonlinear TMP
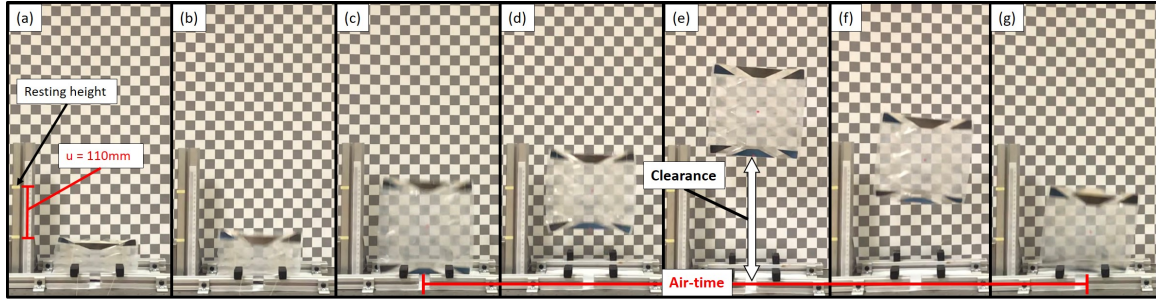
(b) Jump experiment with linear TMP
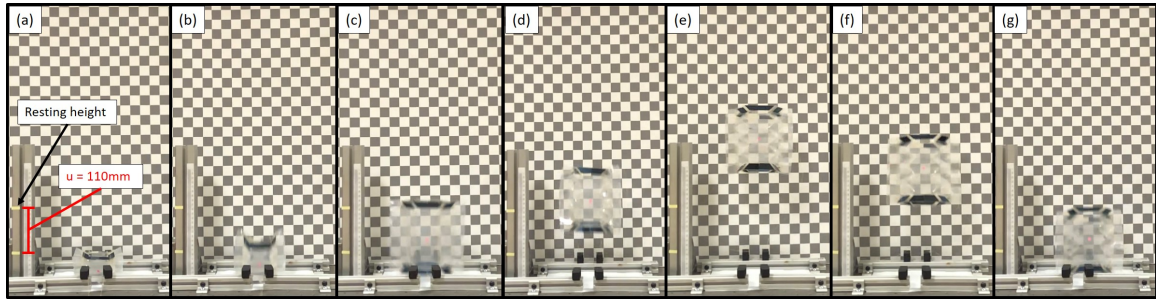
Figure 3.8: Jumping experiments with nonlinear and linear TMP structures with air-time and clearance measurements labeled.

time predicted by the dynamic model is far more accurate than the predicted clearance (the percent error for air-time is less than half that of the clearance for both nonlinear and linear jumpers), both metrics are greatly over-estimated by the model.

Table 3.9: Comparison between theoretical and experimental dynamic performance for the nonlinear jumper

	Nonlinear Jumper		
	Theoretical	Experimental	Percent Error
Air-time [s]	0.531 s	0.461 s	15.22%
Clearance [mm]	359.9 mm	259.7 mm	38.58%

One possible explanation deals with the way in which the mass of the TMP structure is used in the dynamic model. The total mass of the PET sheets is treated as a point mass at either end of the structure, resulting in an increase in the amplitude of oscillations in the model during the jump. Because the maximum clearance is dependent on the height of the lower mass, oscillations of greater amplitude will result in greater predicted clearance values. The air-time, however, depends only on the amount of energy stored in the structure and the overall mass of the structure – the

31

Table 3.10: Comparison between theoretical and experimental dynamic performance for the linear jumper

	Linear Jumper		
	Theoretical	Experimental	Percent Error
Air-time [s]	0.518 s	0.423 s	22.48%
Clearance [mm]	366.8 mm	230.6 mm	59.04%

oscillations of the jumper do not affect this metric, therefore leading to better agreement with the experimental results.

However, the error between the dynamic model and the experimental results is still significant for both performance metrics and both jumper configurations. One theory that explains the discrepancy is the structural damping that exists within the TMP structure during take-off and subsequent oscillations while airborne. Table 3.3 in Section 3.1.2 shows that even with the use of the PALEO creases, the TMP bellow is still not perfectly efficient and exhibits structural damping during a compression cycle. Due to the complexity in approximating the magnitude of structural damping and integrating this quantity into an equation of motion, the presence of damping was instead approximated using a viscous damping term in the equation of motion. The equations of motion (3.3), (3.4), and (3.5) were revised to include a damping constant C, as shown below.

$$m_2 \ddot{y}_2 = F - m_2 g - C \dot{y}_2 \tag{3.3}$$

$$m_1 \ddot{y}_1 = -F - m_1 g + C \left(\dot{y}_2 - \dot{y}_1 \right) \tag{3.4}$$

$$m_2 \ddot{y}_2 = F - m_2 g - C \left(\dot{y}_2 - \dot{y}_1 \right) \tag{3.5}$$

In order to relate the amount of damping observed in the quasi-static compression cycle tests, a technique from Blandon *et. al.* [43] was used to relate the amount of dissipated energy to an equivalent damping ratio ζ_{eq}. This damping ratio was then used in conjunction with the natural frequency of the structure to estimate the magnitude of the damping constant C, as shown in Equation (3.8). In Equation (3.7), the spring stiffness k was treated as a constant stiffness equal to

that of the ideal linear spring plotted in Figure 3.7.

$$\zeta_{eq} = \frac{E_{dissipated}}{4\pi E_{stored}} \tag{3.6}$$

$$\omega_n = \sqrt{\frac{k(m_1 + m_2)}{m_1 m_2}} \tag{3.7}$$

$$C = 2(m_1 + m_2)\zeta_{eq}\omega_n \tag{3.8}$$

Table 3.11: Updated comparison between theoretical and experimental dynamic performance for the nonlinear jumper

	Nonlinear Jumper $(C = 0.0657$ [N/s]$)$		
	Theoretical	Experimental	Percent Error
Air-time [s]	0.495 s	0.461 s	7.44%
Clearance [mm]	314.8 mm	259.7 mm	21.21%

Table 3.12: Updated comparison between theoretical and experimental dynamic performance for the linear jumper

	Linear Jumper $(C = 0.0907$ [N/s]$)$		
	Theoretical	Experimental	Percent Error
Air-time [s]	0.484 s	0.423 s	14.39%
Clearance [mm]	293.7 mm	230.6 mm	27.36%

Tables 3.11 and 3.12 show the revised dynamic performance metrics with the introduction of the calculated damping constant for the nonlinear and linear jumpers, respectively. The dynamic model still overestimates the airtime and clearance of the jumper for both the nonlinear and linear configurations, but the error has been significantly reduced. We still see relatively large error in the clearance approximation due to the TMP mass being applied at the end-points as previously discussed, but the air-time approximation is acceptable at under 10% for the nonlinear jumper and under 15% for the linear jumper. The greater error observed in the dynamic data for the linear jumper may also be due in-part to the amount of error observed in the theoretical quasi-static model. Table 3.5 shows an discrepancy of 11.34% in the energy storage for the linear TMP, whereas

the nonlinear TMP exibits an error of only 2.77%. This may further explain the greater amount of error in the dynamic results for the linear TMP relative to the nonlinear TMP.

Chapter 4

Conclusions

In this study, we demonstrate the effectiveness of utilizing origami to design and fabricate an optimized jumping mechanism which outperforms a generic linear elastic element in dynamic experiments. The force-displacement equation developed in [38] is used in conjunction with crease stiffness modifications proposed in [40] to derive a theoretical force-displacement curve that more accurately models the behavior of the TMP structure. We simulate the dynamic response of a TMP jumping mechanism consisting of the TMP bellow with two end-point masses and identify two performance metrics: air-time and clearance. These metrics are then used as objectives to be maximized during a multi-objective optimization procedure, where the NSGA-II algorithm is used to identify the geometric parameters of the TMP that result in improved dynamic performance. In addition to the optimized TMP design, an additional TMP is fabricated to act as a representative linear spring.

We identify two main sources of hysteresis observed during the compression cycle of a TMP structure. The hysteresis due to friction is minimized through the use of PTFE (Teflon) sheets at both ends of the structure. The hysteresis due to plastic deformation at the creases of the structure is minimized through the use of the PALEO technique, in which the PET sheets are perforated and annealed to relax the internal stresses of the structure. We measure the torsional stiffness of various perforation configurations in order to change the stiffness of the main-folds and sub-folds in the TMP structure. The crease stiffness data is used to stiffen the sub-folds and weaken the main-folds in the optimized TMP, and also to weaken the sub-folds and stiffen the main-folds in the linear TMP.

We further validate the force-displacement model in Equation (2.1) by computing the per-

cent error in energy storage when compared to the optimized and linear TMP structures. The end-point masses are secured to the facets of the upper and lower unit cells of both structures, and the dynamic performance of both configurations is experimentally measured over ten trials. Upon observation of significant damping effects in the experimental study, we update the dynamic model to include a damping constant that is directly related to the magnitude of the hysteresis loop observed for each structure. The updated dynamic model shows better agreement with the dynamic performance measured in the experiments. Furthermore, we show that the optimized TMP structure is capable of providing significant improvement in the air-time and clearance of a jumping mechanism when compared to a standard linear elastic element.

Future work may consist of further reduction in the hysteresis loop during a compression cycle in an attempt to obtain experimental results that more closely align with the idealized case considered in the dynamic model. The PALEO crease configurations considered in this study were not exhaustive, so there may be cut patterns that enable greater efficiencies in the form of a smaller hysteresis loop. This study is intended to provide the foundation for an energy storage mechanism to be used in a jumping robot. Therefore, implementation into a robotic system is still required. One of the benefits of using TMP origami as the jumping mechanism is that the structure is scalable and can therefore be sequenced in parallel to fabricate a "leg" for use in hopping. We present these results in an effort to expand the tools available to robotics engineers and to give rise to a new generation of exploratory robots.

Appendices

Appendix A Force-Displacement Function

```matlab
1  function [F,theta_M,theta_G,theta_S] =
2  ForceDisplacement_TMP(u_tot,l,m,c,d,alpha,N,km_PUL,...
3      ks_PUL,theta_M0,theta_S1,theta_S2,theta_M1,theta_M2)
4
5  format long
6
7  %Initial angle states
8  theta_G0 = 2*atand(tand(alpha)*cosd(theta_M0)); %[deg]
9  theta_S0 = acosd(sind(0.5*theta_G0)/sind(alpha)); %[deg]
10
11 %Define angles thru bending
12 theta_M = asind(sind(theta_M0) - (u_tot/(N*d))); %[deg]
13 theta_G = 2*atand(tand(alpha)*cosd(theta_M)); %[deg]
14 theta_S = acosd(sind(0.5*theta_G)/sind(alpha)); %[deg]
15
16 %Compute total main- and sub-fold stiffnesses
17 km = km_PUL*(l+m+c); %[N*m/rad]
18 ks = ks_PUL*(d/sind(alpha)); %[N*m/rad]
19
20 % Calculate Reaction Forces (Sub-Folds)
21 if (theta_S < theta_S1)
22     theta_Sr = theta_S*(pi/180);
23     theta_S0r = theta_S0*(pi/180);
24     theta_S1r = theta_S1*(pi/180);
25     theta_Mr = theta_M*(pi/180);
26     theta_Gr = theta_G*(pi/180);
27
28     Ls = (-32*((cos(0.5*theta_Gr))^3)*sin(theta_Mr))/...
29         (d*cos(theta_Mr)*cosd(alpha)*sin(theta_Sr));
30     % Increase in rotational stiffness
31     ks_inflated = ks*(sec((pi*(theta_Sr-theta_S1r))/...
32         (3.5*theta_S1r)))^2;
33     % Force calculation
34     Fs = Ls*ks_inflated*(theta_Sr-theta_S0r);
35
```

```matlab
36   elseif (theta_S > theta_S2)
37       theta_Sr = theta_S*(pi/180);
38       theta_S0r = theta_S0*(pi/180);
39       theta_S2r = theta_S2*(pi/180);
40       theta_Mr = theta_M*(pi/180);
41       theta_Gr = theta_G*(pi/180);
42
43       Ls = (-32*((cos(0.5*theta_Gr))^3)*sin(theta_Mr))/...
44           (d*cos(theta_Mr)*cosd(alpha)*sin(theta_Sr));
45       % Increase in rotational stiffness
46       ks_inflated = ks*(sec((pi*(theta_Sr-theta_S2r))/...
47           (2*pi-3.5*theta_S2r)))^2;
48       % Force calculation
49       Fs = Ls*ks_inflated*(theta_Sr-theta_S0r);
50   else
51       theta_Sr = theta_S*(pi/180);
52       theta_S0r = theta_S0*(pi/180);
53       theta_Mr = theta_M*(pi/180);
54       theta_Gr = theta_G*(pi/180);
55
56       Ls = (-32*(cos(0.5*theta_Gr))^3*sin(theta_Mr))/...
57           (d*cos(theta_Mr)*cosd(alpha)*sin(theta_Sr));
58       Fs = Ls*ks*(theta_Sr-theta_S0r);
59
60   end
61
62   % Calculate Reaction Forces (Main-Folds)
63   if (theta_M < theta_M1)
64       theta_Mr = theta_M*(pi/180);
65       theta_M0r = theta_M0*(pi/180);
66       theta_M1r = theta_M1*(pi/180);
67
68       Lm = (-32*(N-1)*.4)/(N*d*cosd(theta_M));
69       % Increase in rotational stiffness
70       km_inflated = km*sec((pi*(theta_Mr-theta_M1r))/...
71           (3.5*theta_M1r))^2;
72       % Force calculation
73       Fm = Lm*km_inflated*(theta_Mr-theta_M0r);
74   elseif (theta_M > theta_M2)
```

```matlab
75
76     theta_Mr = theta_M*(pi/180);
77     theta_M0r = theta_M0*(pi/180);
78     theta_M2r = theta_M2*(pi/180);
79
80     Lm = (-32*(N-1)*.4)/(N*d*cosd(theta_M));
81     % Increase in rotational stiffness
82     km_inflated = km*(sec((pi*(theta_Mr-theta_M2r))/...
83         (2*pi-3.5*theta_M2r)))^2;
84     % Force calculation
85     Fm = Lm*km_inflated*(theta_Mr-theta_M0r);
86 else
87     theta_Mr = theta_M*(pi/180);
88     theta_M0r = theta_M0*(pi/180);
89
90     Lm = (-32*(N-1)*.4)/(N*d*cos(theta_Mr));
91     Fm = Lm*km*(theta_Mr-theta_M0r);
92 end
93
94 F = [Fm,Fs];
95 end
```

Appendix B   Equations of Motion

```matlab
%% Pre-Jump EoM
function [dydt] = EoM_prejump(t,y,l,m,c,d,alpha,N,km,ks,...
    theta_M0,theta_S1,theta_S2,theta_M1,theta_M2,l_0,m2,g,C)
[F] = ForceDisplacement_TMP(-(y(1)-l_0),l,m,c,d,alpha,N,...
    km,ks,theta_M0,theta_S1,theta_S2,theta_M1,theta_M2);
dydt = zeros(2,1);
dydt(1) = y(2);
dydt(2) = (1/m2)*F - g - (1/m2)*C*y(2);
```

```matlab
%% Post-Jump EoM
function dydt = EoM_postjump(t,y,l,m,c,d,alpha,N,km,ks,...
    theta_M0,theta_S1,theta_S2,theta_M1,theta_M2,l_0,...
    m1,m2,g,C)
[F] = ForceDisplacement_TMP(-(y(1)-y(3)-l_0),l,m,c,d,...
    alpha,N,km,ks,theta_M0,theta_S1,theta_S2,...
    theta_M1,theta_M2);
dydt = zeros(4,1);
dydt(1) = y(2);
dydt(2) = 1/m2*F - g - (1/m2)*C*(y(2)-y(4));
dydt(3) = y(4);
dydt(4) = -1/m1*F - g + (1/m1)*C*(y(2)-y(4));
```

Appendix C   Solving Equations of Motion

```matlab
1  function [F] = DynamicBehavior(x)

2

3  clc

4

5  % Initialize Parameters for ForceDisplacement_TMP function
6  N = x(1); %number of unit cells [-]
7  c = x(2); %[m]
8  d = x(3); %[m]
9  l = x(4); %[m]
10 m = x(5); %[m]
11 alpha = x(6); %[deg]

12

13 % Masses
14 % mass 1 [kg] first number is attached mass
15 m1 = 0.017713 + 0.000127*(c+l+m)*2*d*N*1383.9952;
16 % mass 2 [kg] first number is attached mass
17 m2 = 0.017615 + 0.000127*(c+l+m)*2*d*N*1383.9952;

18

19 % Crease Stiffness
20 % main-fold stiffness [N*m/rad]
21 km = (0.001113232392549 / 0.06);
22 % sub-fold stiffness [N*m/rad]
23 ks = (0.005678477536300 / 0.06);

24

25 g = 9.81; %gravitational acceleration [m/s^2]

26

27 theta_M0 = 60; %resting main fold angle [deg]
28 FR = 0.75; %folding ratio [-]

29

30 %Angle limits for crease stiffness inflation
31 theta_S1 = 38; %[deg]
32 theta_S2 = 70; %[deg]
33 theta_M1 = 38; %[deg]
34 theta_M2 = 70; %[deg]

35
```

```matlab
36  % % Resting height and initial compression height
37  l_0 = N*d*sind(theta_M0); %total resting height [m]
38  l_max = N*d; %max extension length
39  y_0 = N*d*sind(90*(1-FR)); %initial compression height [m]
40  u_0 = (y_0-l_0); %inital displacement [m]
41
42
43  %% Pre-Jump Phase
44  % Define damping constant
45  C = 0;
46
47  % Solve first ode
48  [t1,y_pre] = ode45(@(t2,y2) EoM_prejump(t2,y2,l,m,c,d,...
49  alpha,N,km,ks,theta_M0,theta_S1,theta_S2,theta_M1,theta_M2,...
50  l_0,m2,g,C),[0,0.5],[y_0,0],odeset('Refine',10));
51
52  y_pre(:,1) = real(y_pre(:,1));
53
54  % Read out tension force during extension
55  position = linspace(l_0,l_max,1000);
56  for i = 1:length(position)
57      F_count(i,1) = ForceDisplacement_TMP...
58      (-(position(i)-l_0),l,m,c,d,alpha,N,km,ks,theta_M0,...
59      theta_S1,theta_S2,theta_M1,theta_M2);
60  end
61  F_count = F_count(1:end-1,:);
62  position = position(:,1:end-1);
63
64  % Locate the displacement at which jumping occurs
65  u_jump = interp1(F_count,-(position-l_0),-m1*g); %[m]
66
67  % Find Y2 coordinate at which jumping occurs
68  y2_jump = -u_jump+l_0; %[m]
69
70  % Locate the element position of the jump
71  loc_count = 1;
72  while y_pre(loc_count,1) < y2_jump
73      loc_count = loc_count+1;
74  end
```

43

```
75
76  % Time of jump averaged ("at" or "just after" the jump)
77  t_jump = mean([t1(loc_count),t1(loc_count-1)]);
78
79  %% Post-Jump Phase
80
81  % Define initial conditions for post-jump phase
82  ic_pos = y2_jump;
83  ic_vel = mean([y_pre(loc_count,2),y_pre(loc_count+1,2)]);
84  ic_time = t_jump;
85  ic = real([ic_pos; ic_vel; 0; 0]);
86
87  % Solve post-jump system
88  [t2,y_post] = ode45(@(t2,y2) EoM_postjump(t2,y2,l,m,c,d,...
89  alpha,N,km,ks,theta_M0,theta_S1,theta_S2,theta_M1,theta_M2,...
90  l_0,m1,m2,g,C),[ic_time 4],ic);
91
92  % Convert complex values to real values
93  y_post(:,1) = real(y_post(:,1));
94  y_post(:,3) = real(y_post(:,3));
95
96  % Find the time of landing
97  land_count = find(y_post(:,3) == max(y_post(:,3)));
98  while y_post(land_count,3)≥0
99      land_count = land_count+1;
100 end
101
102 t_land = mean([t2(land_count),t2(land_count+1)]);
103
104 y1_tot = [zeros(loc_count,1);y_post(1:land_count+1,3)];
105 y2_tot = [y_pre(1:loc_count,1);y_post(1:land_count+1,1)];
106 t_tot = [t1(1:loc_count);t2(1:land_count+1)];
107
108 F(1) = (t_land - t_jump);
109 AirTime = F(1)
110
111 maxCoM = (max(0.5*(y1_tot+y2_tot)))
112 F(2) = max(y1_tot);
113 Clearance = F(2)
```

```matlab
114
115 figure
116 hold on
117 plot(t_tot,y1_tot,'r-')
118 plot(t_tot,y2_tot,'b-')
119 plot(t_tot,0.5*(y1_tot+y2_tot),'k-')
120 plot(linspace(0,t_land,100),l_0*ones(1,100),'k--')
121 legend('M1','M2','Center of Mass','Resting Height',...
122 'Location','eastoutside')
123 xlabel('Time (t) [s]')
124 ylabel('Y-coordinate (Y_1, Y_2) [m]')
125 title('Dynamic Performance of TMP Jumper')
126 end
```

Bibliography

[1]   M. Shneier and R. Bostelman. "Literature Review of Mobile Robots for Manufacturing". In: *National Institute of Standards and Technology* 8022 (2015). DOI: http://dx.doi.org/10. 6028/NIST.IR.8022.

[2]   A. Shukla and H. Karki. "Application of robotics in onshore oil and gas industry - A review Part I". In: *Robotics and Autonomous Systems* 75 (2015), pp. 490–507. DOI: https://doi. org/10.1016/j.robot.2015.09.012.

[3]   R. Bogue. "Robots in the nuclear industry: a review of technologies and applications". In: *Industrial Robot* 38.2 (2011), pp. 113–118. DOI: https://doi-org.libproxy.clemson.edu/ 10.1108/01439911111106327.

[4]   P. Chua, T. Ilschner, and D. Caldwell. "Robotic manipulation of food products – a review". In: *Industrial Robot* 30.4 (2003), pp. 345–354. DOI: https://doi.org/10.1108/ 01439910310479612.

[5]   N. Reddy et al. "A Critical Review on Agricultural Robots". In: *International Journal of Mechanical Engineering and Technology* 7.4 (2016), pp. 183–188. DOI: http://www.iaeme. com/ijmet/issues.asp?JType=IJMET&VType=7&IType=4.

[6]   F. Benitti. "Exploring the educational potential of robotics in schools: A systematic review". In: *Computers and Education* 58.3 (2011), pp. 978–988. DOI: https://doi.org/10.1016/j. compedu.2011.10.006.

[7]   R. van den Berghe et al. "Social Robots for Language Learning: A Review". In: *Review of Educational Research* 89.2 (2018), pp. 259–295. DOI: https://doi-org.libproxy.clemson. edu/10.3102/0034654318821286.

[8]   P. Jamwal, S. Hussain, and S. Xie. "Review on design and control aspects of ankle rehabilitation robots." In: *Disability Rehabilitation: Assistive Technology* 10.2 (2015), pp. 93–101. DOI: http: //dx.doi.org.libproxy.clemson.edu/10.3109/17483107.2013.866986.

[9]   H. Robinson, B. MacDonald, and E. Broadbent. "The Role of Healthcare Robots for Older People at Home: A Review". In: *International Journal of Social Robotics* 6 (2014), pp. 575– 591. DOI: https://doi-org.libproxy.clemson.edu/10.1007/s12369-014-0242-2.

[10] A. Blokhin et al. "The Analytical Review of the Condition of Heavy Class Military and Dual-Purpose Unmanned Ground Vehicle". In: *MATEC Web of Conferences* 26.04002 (2015). DOI: https://doi.org/10.1051/matecconf/20152604002.

[11] V. Kunchev et al. "Path Planning and Obstacle Avoidance for Autonomous Mobile Robots: A Review". In: *Lecture Notes in Computer Science* 4252 (2006), pp. 537–544.

[12] Z. Wang and H. Gu. "A review of locomotion mechanisms of urban search and rescue robot". In: *Industrial Robot* 34.5 (2007), pp. 400–411. DOI: https://doi.org/10.1108/01439910710774403.

[13] A. Reddy, B. Kalyan, and C. Murthy. "Mine Rescue Robot System – A Review". In: *Procedia Earth and Planetary Science* 11 (2015), pp. 457–462. DOI: https://doi.org/10.1016/j. proeps.2015.06.045.

[14] H. Zhuang et al. "A review of heavy-duty legged robots". In: *Science China Technological Sciences* 57.2 (2013), pp. 298–314. DOI: https://doi.org/10.1007/s11431-013-5443-7.

[15] S. Dubey, M. Prateek, and M. Saxena. "Robot Locomotion – A Review". In: *International Journal of Applied Engineering Research* 10.3 (2015), pp. 7357–7369.

[16] N. Cherouvim and E. Papadopoulos. "Energy saving passive-dynamic gait for a one-legged hopping robot". In: *Robotica* 24 (2006), pp. 491–498. DOI: https://doi.org/10.1017/S026357470500250X.

[17] A. Sayyad, B. Seth, and P. Seshu. "Single-legged hopping robotics research — A review". In: *Robotica* 25.5 (2007), pp. 587–613. DOI: https://doi.org/10.1017/S0263574707003487.

[18] H. Vu et al. "Improving Energy Efficiency of Hopping Locomotion by Using a Variable Stiffness Actuator". In: *IEEE/ASME Transactions on Mechatronics* 21.1 (2016), pp. 472–486. DOI: https://doi.org/10.1109/TMECH.2015.2428274.

[19] J. Zhao et al. "MSU Jumper: A Single-Motor-Actuated Miniature Steerable Jumping Robot". In: *IEEE Transactions on Robotics* 29.3 (2013), pp. 602–614. DOI: https://doi.org/10.1109/TRO.2013.2249371.

[20] J. Albro and J. Bobrow. "Optimal motion primitives for a 5 DOF experimental hopper". In: *IEEE International Conference on Robotics and Automation* (2001). DOI: https://doi.org/10.1109/ROBOT.2001.933181.

[21] S. Sadeghi et al. "The Effect of Nonlinear Springs in Jumping Mechanisms". In: *ASME Dynamic Systems and Control Conference* DSCC2018-8969 (2018). DOI: https://doi.org/10.1115/DSCC2018-8969.

[22] U. Scarfogliero, C. Stefaninia, and P. Dario. "The use of compliant joints and elastic energy storage in bio-inspired legged robots". In: *Mechanism and Machine Theory* 44 (2009), pp. 580–590. DOI: https://doi.org/10.1016/j.mechmachtheory.2008.08.010.

[23] J. Zhang et al. "An indoor security system with a jumping robot as the surveillance terminal". In: *IEEE Transactions on Consumer Electronics* 57.4 (2011), pp. 1774–1781. DOI: https://doi.org/10.1109/TCE.2011.6131153.

[24] J. Zhao et al. "Design and testing of a controllable miniature jumping robot". In: *IEEE/RSJ International Conference on Intelligent Robots and Systems* (2010). DOI: https://doi.org/10.1109/ROBOT.2008.4543214.

[25] H. Tsukagoshi et al. "Numerical Analysis and Design for a Higher Jumping Rescue Robot Using a Pneumatic Cylinder". In: *Journal of Mechanical Design* 127.2 (2005), pp. 308–314. DOI: https://doi.org/10.1115/1.1825440.

[26] S. Dubowsky et al. "Hopping mobility concept for search and rescue robots". In: *Industrial Robot* 35.3 (2008), pp. 238–245. DOI: https://doi.org/10.1108/01439910810868561.

[27] A. Yamada et al. "An asymmetric robotic catapult based on the closed elastica for jumping robot". In: *IEEE International Conference on Robotics and Automation* (2008). DOI: https://doi.org/10.1109/ROBOT.2008.4543214.

[28] A. Yamada et al. "A compact jumping robot utilizing snap-through buckling with bend and twist". In: *IEEE/RSJ International Conference on Intelligent Robots and Systems* (2010). DOI: https://doi.org/10.1109/IROS.2010.5652928.

[29] P. Fiorini and J. Burdick. "The Development of Hopping Capabilities for Small Robots". In: *Autonomous Robots* 14.2-3 (2003), pp. 239–254. DOI: https://doi.org/10.1023/A:1022239904879.

[30] E. Filipov, T. Tachi, and G. Paulinoa. "Origami tubes assembled into stiff, yet reconfigurable structures and metamaterials". In: *Proceedings of the National Academy of Sciences* 112.40 (2015), pp. 12321–12326. DOI: https://doi.org/10.1073/pnas.1509465112.

[31] S. Felton et al. "A method for building self-folding machines". In: *Science* 345.6197 (2014), pp. 644–646. DOI: https://doi.org/10.1126/science.1252610.

[32] M. Johnson et al. "Fabricating biomedical origami: a state-of-the-art review". In: *International Journal of Computer Assisted Radiology and Surgery* 12 (2017), pp. 2023–2032. DOI: https://doi.org/10.1007/s11548-017-1545-1.

[33] P. Wang et al. "The Beauty and Utility of DNA Origami". In: *Chem* 2.3 (2017), pp. 359–382. DOI: https://doi.org/10.1016/j.chempr.2017.02.009.

[34] H. Fang, S. Li, and K. Wang. "Self-locking degree-4 vertex origami structures". In: *The Royal Society* 472.2195 (2016). DOI: https://doi.org/10.1098/rspa.2016.0682.

[35] S. Li et al. "Architected Origami Materials: How Folding Creates Sophisticated Mechanical Properties". In: *Advanced Materials* 31.5 (2018). DOI: https://doi.org/10.1002/adma.201805282.

[36] H. Fang et al. "Dynamics of a bistable Miura-origami structure". In: *Physical Review* 95.5 (2017). DOI: https://doi.org/10.1103/PhysRevE.95.052211.

[37] S. Sadeghi and S. Li. "Harnessing the Quasi-Zero Stiffness From Fluidic Origami for Low Frequency Vibration Isolation". In: *ASME Conference on Smart Materials, Adaptive Structures and Intelligent Systems* (2017). DOI: https://doi.org/10.1115/SMASIS2017-3754.

[38] H. Yasuda and J. Yang. "Reentrant Origami-Based Metamaterials with Negative Poisson's Ratio and Bistability". In: *American Physical Society* 114.185502 (2015). DOI: http://dx.doi.org/10.1103/PhysRevLett.114.185502.

[39] Y. Klett. "PALEO: Plastically Annealed Lamina Emergent Origami". In: *American Society of Mechanical Engineers* 5B: 42nd Mechanisms and Robotics Conference.DETC2018-85983 (2018). DOI: https://doi.org/10.1115/DETC2018-85983.

[40] K. Liu and G. H. Paulino. "Nonlinear Mechanics of Non-Rigid Origami: an Efficient Computational Approach". In: *Royal Society Publishing* 473.20170348 (2017). DOI: http://dx.doi.org/10.1098/rspa.2017.0348.

[41] K. Deb et al. "A Fast and Elitist Multiobjective Genetic Algorithm: NSGA-II". In: *IEEE Transactions on Evolutionary Computation* 6.2 (2002), pp. 182–197.

[42] B. Sargent et al. "Heat Set Creases in Polyethylene Terephthalate (PET) Sheets to Enable Origami-based Applications". In: *Smart Materials and Structures* 28.11 (2019), p. 115047. DOI: https://doi.org/10.1088/1361-665X/ab49df.

[43] C. Blandon and M. Priestley. "EQUIVALENT VISCOUS DAMPING EQUATIONS FOR DIRECT DISPLACEMENT BASED DESIGN". In: *Journal of Earthquake Engineering* 9.sup2 (2010), pp. 257–278. DOI: https://doi.org/10.1142/S1363246905002390.